This article has been accepted for publication in a future issue of this journal, but has not been fully edited. Content may change prior to final publication. Citation information: DOI 10.1109/JSEN.2017.2756905, IEEE Sensors Journal

Energization-Status Identification of Three-Phase Three-Core Shielded Distribution Power Cables Based on Non-Destructive Magnetic Field Sensing

Ke ZHU, *Student Member, IEEE*, W. K. LEE, and Philip W. T. PONG*, *Senior Member, IEEE*

***Abstract*— Three-phase three-core distribution power cables are widely deployed in power distribution networks and are continually being extended to address the ever-increasing power demand in modern metropolises. Unfortunately, there are high risks for the repair crew to operate on energized distribution power cables which can cause deadly consequences such as electrocution and explosion. The predominant energization-status identification techniques used today are either destructive or only applicable to un-shielded power cables. Moreover, the background interferences affect the sensing technique reliability. In this paper, we have developed a non-destructive energization-status identification technique to identify energized three-phase three-core distribution power cables by measuring magnetic fields around the cable surface. The analysis shows that the magnetic-field-distribution pattern as a function of azimuth around the cable surface of the energized (current- or voltage-energized) three-phase three-core distribution power cable is distinguishable from the de-energized one. The non-idealities of phase currents and cable geometry were also discussed, and the proposed method still works under these circumstances. The sensing platform for implementing this technique was developed accordingly, consisting of magnetoresistive (MR) sensors, a triple-layered magnetic shielding and a data acquisition system. The technique was demonstrated on a 22-kV three-phase three-core distribution power cable, and the energized status of the cable can be successfully identified. The proposed technique does not damage cable integrity by piercing the cable, or exposing the repair crew to hazardous high-voltage conductors. The platform is easy to operate and it can significantly improve the situational awareness for the repair crew, and enhance the stability of power distribution networks.**

***Index Terms*— three-phase three-core distribution power cable, energized status, magnetic sensing, distribution power network**

I. INTRODUCTION

THREE-PHASE three-core distribution power cables are widely deployed in the power distribution system which acts as the last link in the chain of supplying the power to the customers. Though these power cables are less susceptible by weather-related outages (e.g., thunderstorms, heavy snows [1-3]) as they are typically hidden underground, maintenance tasks are regularly performed by the repair crew to inspect defective cables (e.g., insulation deterioration, mechanical cracks and even wire break points), or to splice power cables for re-structuring the distribution power networks [4-7]. Nonetheless, there are high risks for the repair crew to operate on energized distribution power cables (i.e., cables that connected with the high-voltage power supply). For the repair crew conducting on-site work, they must be highly alerted of these energized power cables because contacting with a high-voltage conductor can cause deadly consequences such as explosion and flashover. Due to the continued distribution power network expansion, administrative changes, poor record-keeping, or other reasons, the topological representation of the power distribution network may not be completely accurate and up-to-date. Therefore, it is difficult for the repair crew to locate and identify the energized three-phase three-core distribution power cables accurately and safely based on the information from the control station when implementing the onsite tasks [8].

Researchers and industrial companies have developed a handful of techniques to identify the energized power cables for safeguarding the safety of the repair crew [9-11]. However, the predominant detection techniques today are either destructive in nature or only applicable for the un-shielded power cables. The SPIKE tool [12], for example, pierces through the cable insulation to make electrical contact with the internal conductor and thus inextricably damages the cable. The penetration into the cable not only causes irreversible damage to the integrity of the cable, but also exposes workers to a potentially hazardous situation with high-voltage conductors. Robots have been developed to replace the human work of penetrating the cables, but the damage to the power cables is still unavoidable [13, 14]. Though a handful of non-destructive techniques have been developed for improving the situation, the strong dependence of the cable type (i.e., un-shielded power cable) limits their usage. Notably, electric fields are generated from the energized conductors and the related technique is developed [15, 16]. Nevertheless, the detection of the electric field is only applicable for un-shielded (i.e. without metallic sheath) distribution power cables as the electric fields terminate on the earthed metallic sheath of the shielded cables. Moreover, since the onsite environment is very complicated with background interferences, the reliability of devices can be adversely affected. For instance, a technique of attaching fiber optic acoustic sensors on the cable surface was developed based on the detection of acoustic vibrations that are associated with the energized cables [17]. However, the de-energized cables can be mistaken as the energized ones since the optical fiber sensing system is not immune to ambient power-line-frequency electro-magnetic noises and thus it may provide unreliable results. Therefore, it is worthwhile to develop a non-destructive and reliable technique applicable for identifying the energized cables for both shielded and un-shielded cables.

This research is supported by the Seed Funding Program for Basic Research, Seed Funding Program for Applied Research and Small Project Funding Program from the University of Hong Kong, ITF Tier 3 funding (ITS-104/13, ITS-214/14), and University Grants Committee of HK (AoE/P-04/08). The authors would like to thank the Hongkong Electric Company Limited, Hong Kong for assisting the onsite experiment.
*Corresponding email: ppong@eee.hku.hk.

This article has been accepted for publication in a future issue of this journal, but has not been fully edited. Content may change prior to final publication. Citation information: DOI 10.1109/JSEN.2017.2756905, IEEE Sensors Journal

Magnetic sensing for identifying the energized cables is a promising solution [18, 19]. Firstly, the magnetic fields are emanated outside the energized cables both for current-energized (i.e., with load current) and voltage-energized statuses (i.e., the charging current exists when the cable is disconnected from the load but remains connected with the power supply) [20, 21]. This makes the non-contact detection possible without the need to penetrate into the cable, which is beneficial to both cable integrity and personnel safety. Secondly, the magnetic fields are still measurable around the shielded cable since the metallic sheath is not a high-permeability material [22, 23]. Furthermore, the ambient magnetic interference can be effectively eliminated by a magnetic shielding to ensure the accuracy and reliability of this technique. Therefore, it can be feasible and reliable to identify the shielded energized cables by non-destructive magnetic sensing.

In this paper, a novel non-destructive energization-status identification technique based on the recognition of RMS magnetic-field-distribution pattern as a function of azimuth around the cable surface is proposed for identifying the energized (current- or voltage-energized) three-phase three-core distribution power cables. The content of this paper is as follows. In Section II, the magnetic field distribution patterns of all cable statuses (i.e., current-, voltage- and de-energized) were analyzed. The non-idealities of phase currents and cable geometry were also discussed. Based on the findings, a sensing platform hardware consisting of a magnetoresistive (MR) sensor array and a triple-layered magnetic shielding was designed to measure magnetic field around the cable surface in Section III. In Section IV, the proposed technique was experimentally verified on a 22-kV three-phase three-core distribution power cable in a substation. The final conclusions and future work are presented in Section V.

II. Magnetic Field Distribution of Current-, Voltage-, and De-Energized Three-Phase Three-Core Power Cables

In order to distinguish the energization-status of a three-phase three-core distribution power cable, the RMS magnetic-field-distribution pattern around the cable surface was studied for current-, voltage- and de-energized statuses respectively in this Section. The primary voltages for distribution power cables are 11 and 22 kV in Hong Kong (United States: 7.2, 12.47, 25, and 34.5 kV; United Kingdom, Australia and New Zealand: 11 and 22 kV ; South Africa: 11 kV and 22 kV [24]). In this paper, a typical three-phase three-core armored 22-kV XLPE stranded power cable was demonstrated as an example. Its structure is shown in Fig. 1. Each phase conductor is surrounded by a thin tape screen (also named as Hochstadter shield [25]), which is used to equalize the electrical stress on the insulation. Each tape screen is connected to the metallic sheath by the wires at both ends, and then the wires are grounded. The three-phase three-core conductors are assumed to be ideally equidistant to the cable center. The electromagnetic properties of each component are described by the relative permeability ($\boldsymbol{\mu_r}$), relative permittivity ($\boldsymbol{\epsilon_r}$), and conductivity ($\boldsymbol{\sigma_r}$) as listed in Table. I.

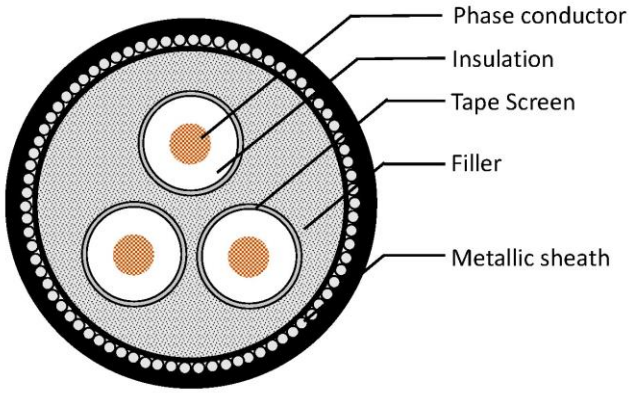

Fig. 1. 22-kV three-phase three-core armored XLPE stranded power cable structure. Radius: (1) phase conductor, 10 mm; (2) tape screen, 15 mm (inner) and 15.5 mm (outer); (3) metallic sheath: 40 mm (inner) and 42 mm (outer).

TABLE I ELECTROMAGNETIC PROPERTY OF 22-KV THREE-PHASE THREE-CORE ARMORED XLPE DISTRIBUTION POWER CABLE

Element	μ_r	ϵ_r	σ_r (s/m)
Phase conductor (Copper)	1.0	1.0	5.8×10^7
Insulation (XLPE)	1.0	2.3	0.0
Tape Screen (Copper)	1.0	1.0	5.8×10^7
Filler (Polypropylene)	1.0	2.3	0.0
Metallic sheath (Steel)	40	1.0	1.1×10^7

A. *Current-energized status*

Only the load currents flow through the phase conductors when the cable is current-energized. The RMS magnetic flux density ($\bar{B}$) at an arbitrary point P (r,θ) around the cable surface is calculated as [26]

$$\bar{B} = \frac{3\mu I}{2\sqrt{2}\pi}\sqrt{\frac{s^4+s^2r^2}{r^6-2s^3r^3\cos(3\theta)+s^6}} \quad (1)$$

where r is the distance from the measurement point to the center, the azimuth of point P is θ with respect to the horizontal direction, and I is the load current of the three-phase power cable (Fig. 2). Eq. (1) shows that the RMS magnetic flux density around the cable surface repeats at an interval of 2/3 π with three crests and troughs as a function of the azimuth of the cable center.

This article has been accepted for publication in a future issue of this journal, but has not been fully edited. Content may change prior to final publication. Citation information: DOI 10.1109/JSEN.2017.2756905, IEEE Sensors Journal

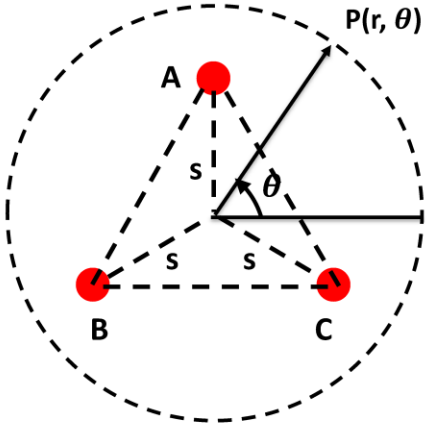

Fig. 2. Magnetic flux density measured at a sensing point (P) around the three-phase three-core conductors (three red dots for phase A, B and C) at various azimuth (θ).

The magnitude of the magnetic flux density around the cable surface with a rated phase current of 1 A was simulated by FEM. The RMS magnetic flux density was about 10 mG around the cable surface (Fig. 3(a)). According to Eq. (1), the RMS magnetic-field-distribution pattern around the cable surface would exhibit a pattern of three peaks and three troughs, which was confirmed by the FEM results as shown in Fig. 3(b). The load current of a current-energized cable is typically ranged from tens to hundreds of amperes (only under some rare extreme cases with very light loading conditions that the load current becomes several amperes) [27-29]. As such, the RMS magnetic-field-distribution pattern around the cable surface typically range from hundreds of mG (i.e., tens amperes of load current) to thousands of mG (i.e., hundreds of amperes of load current). To conclude, the RMS magnetic-field-distribution pattern around the cable surface as a function of the azimuth around the cable surface shows a pattern of three peaks and three troughs with typically magnitude from hundreds or even up to thousands of mG.

B. *Voltage-energized status*

There is no load current flowing on the three-phase three-core conductors when the cable is voltage-energized; however, there are capacitive charging currents which are incurred due to the fact that the phase conductors are still connected to the power source with the alternating voltage [30, 31]. The magnetic field distribution around the cable surface was evaluated from the charging current as follows.

Firstly, the unit resistance of the phase conductor and the tape screen, and the unit capacitance between them were calculated. The resistance is proportional to its electrical resistivity and length, and is inversely proportional to the cross-sectional area. As such, the unit resistance of the phase conductor (R) and the tape screen (r) can be calculated as

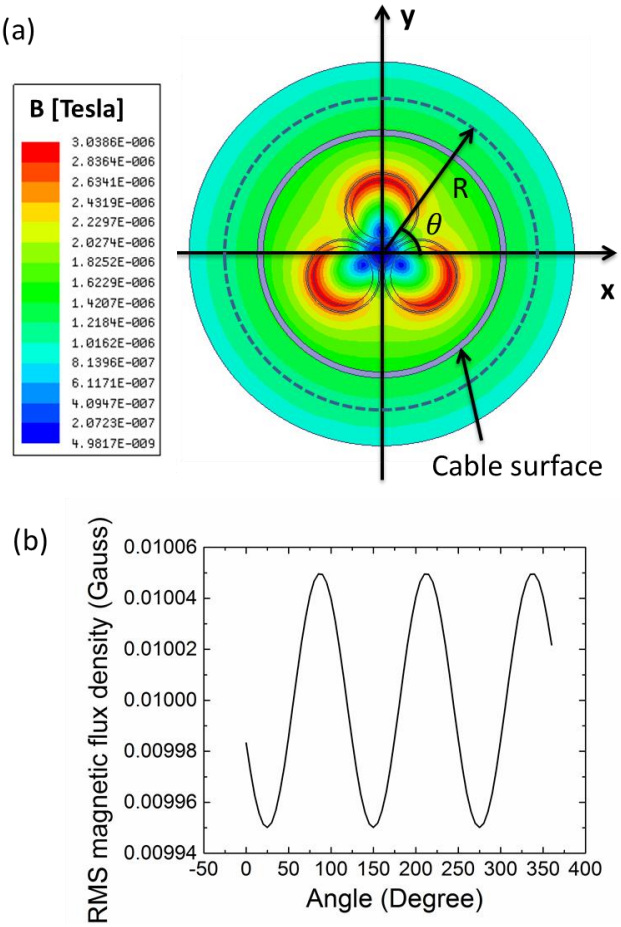

Fig. 3. Magnetic flux density around the current-energized cable surface with a rated current of 1 A simulated by FEM. (a) Magnitude of magnetic field around the cable surface denoted by the color bar. (b) RMS magnetic flux density around the cable: radius (R), 60 mm; azimuth (θ) ranges from 0 to 360°.

$$R = \rho_{pc} \frac{1}{\pi t^2} \tag{2}$$

$$r = \rho_{ts} \frac{1}{\pi({D_o}^2 - {D_i}^2)} \tag{3}$$

where ρ_{pc}, ρ_{ts} are the resistivity of phase conductor and the tape screen, t is the radius of the conductor, and D_i , D_o are the inner and outer radius of the tape screen, respectively. The equivalent capacitor (C_0 in Fig. 4) between the cable phase conductor and the earthed tape screen can be calculated as [32]

$$C_0 = \frac{\varepsilon_r}{41.4 log_{10} \frac{D_i}{t}} \times 10^{-9} \tag{4}$$

where ε_r is the relative permittivity of the insulation between the phase conductor and the tape screen.

Secondly, the charging current distribution and magnitude along the cable was studied. One phase of the power cable (the

This article has been accepted for publication in a future issue of this journal, but has not been fully edited. Content may change prior to final publication. Citation information: DOI 10.1109/JSEN.2017.2756905, IEEE Sensors Journal

other two are only with 120° phase angle differences) was taken as an example by being divided piecewise with the corresponding lumped elements in the equivalent electric circuit model (Fig. 5(a)). The lumped resistors of the phase conductor are denoted as R_1, R_2, …, R_n, the lumped resistors of the tape screen as r_1, r_2, …, r_n, and the lumped equivalent capacitors formed between the phase conductor and the tape screen as C_1, C_2, …, C_n. The charging current for the 600-m length 22-kV power cable (50 Hz) was simulated as an example by dividing the cable into 12 pieces (i.e., n=12). Accordingly, the charging current flowing on the phase conductor (I_{cond}) and the tape screen (I_{ts}) on a certain section (n) can be attained as

$$I_{cond}(n) = I_n \tag{5}$$

$$I_{ts}(n) = I_0 - I_n \tag{6}$$

by solving these equations

$$\left(R_1 + r_1 + \frac{1}{j\omega C_1}\right) I_1 - \frac{1}{j\omega C_1} I_2 - r_1 I_0 = U \tag{7}$$

$$-\frac{1}{j\omega C_{n-1}} I_{n-1} + \left(R_n + r_n + \frac{1}{j\omega C_{n-1}} + \frac{1}{j\omega C_n}\right) I_n - \frac{1}{j\omega C_n} I_{n+1} - r_n I_0 = 0 \text{ (n=2, 3, 4,…, 10, 11)} \tag{8}$$

$$-\frac{1}{j\omega C_{11}} I_{11} + \left(R_{12} + r_{12} + \frac{1}{j\omega C_{11}} + \frac{1}{j\omega C_{12}}\right) I_{12} - r_{12} I_0 = 0 \tag{9}$$

$$-\sum_{i=1}^{12} r_i I_i + \left(\sum_{i=1}^{12} r_i\right) I_0 = 0 \tag{10}$$

where $I(n)(\mathrm{n} = 0, 1, \ldots, 12)$ are the mesh current via the equivalent electric circuit using the mesh current method in Fig. 5(b). Accordingly, the peak values of the charging current on the conductor and tape screen at various positions of the cable (i.e., various distance from the power supply side) are shown in Fig. 6. The charging current on the phase conductor is largest at the power supply side. This is because the charging current on the phase conductor is proportional to the cable length [32, 33]. The charging current of the tape screen at both ends are largest since the electric potential there are the lowest.

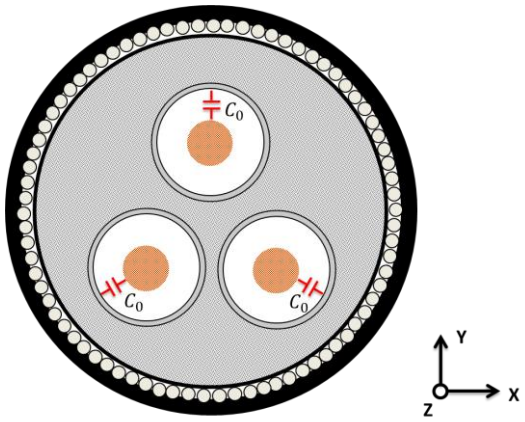

Fig. 4. Capacitor (C_0) formed between phase conductor and earthed tape screen.

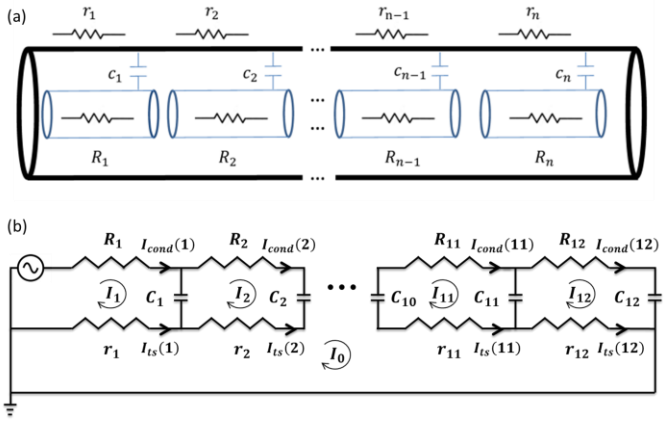

Fig. 5. Equivalent electric model for calculating charging current along cable. (a) One phase is modeled by lumped resistors of phase conductor (R_n), tape screen (r_n) and capacitors between them (C_n). (b) Equivalent electric circuit for calculating charging current via mesh current method.

Finally, the magnetic field distribution around the cable surface measured at various distances from the power supply side were simulated by FEM (Fig. 7). The charging currents flowing on the phase conductor and tape screen were substituted into the FEM model as only the magnetic fields in X-Y plane are measured similarly to those generated from load current (Fig. 4). The results show that the magnitude level of magnetic field around the cable surface varies with the distance from the power supply side. The magnitude is stronger near the power feeder side (~ tens of mG), and it is weaker when it is farther away (~ several mG). Nevertheless, the pattern with three crests and three troughs can be observed irrespective of measuring locations.

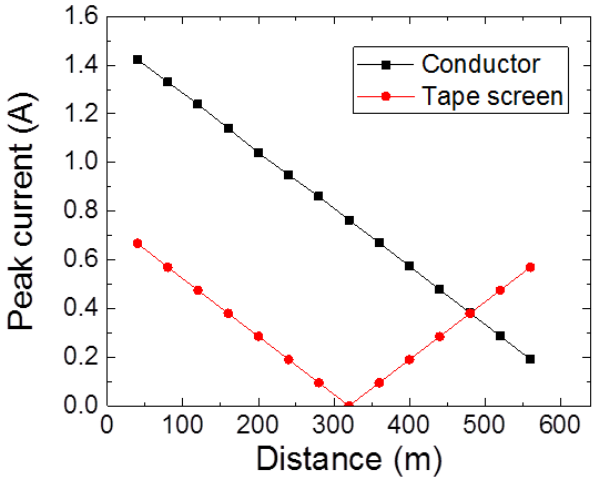

Fig. 6. Charging currents of phase conductor and tape screen at various positions (i.e., various distances from power supply side) on a 600-m power cable.

This article has been accepted for publication in a future issue of this journal, but has not been fully edited. Content may change prior to final publication. Citation information: DOI 10.1109/JSEN.2017.2756905, IEEE Sensors Journal

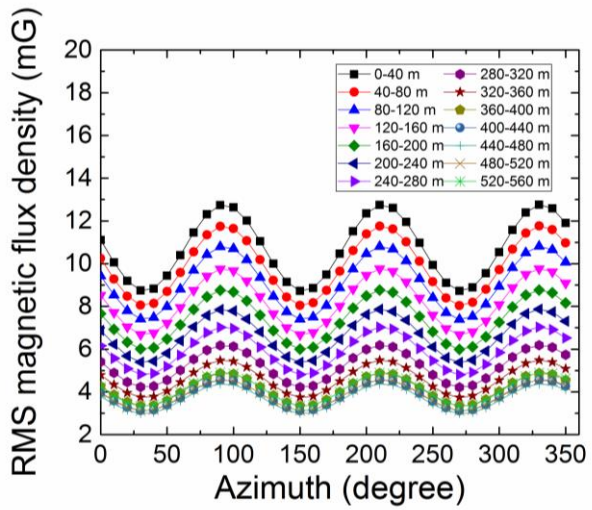

Fig. 7. RMS magnetic-field-distribution pattern around the voltage-energized cable surface (measured at 60mm from the cable center) as a function of azimuth at various distances (0-40 m, 40-80 m, etc.) from power supply side.

The magnitude of the charging current depends on the power supply voltage, cable length and power supply frequency as

$$I_C = 2\pi f C_0 E l \tag{11}$$

where f is the voltage frequency, E is the phase voltage, and l is the cable length [32, 33]). As such, the relations of the magnetic fields with the power supply voltage, cable length, and power supply frequency are studied respectively as follows:

(a) Power supply voltage: according to Eq. (11), the magnitude of the charging current is proportional to the power supply voltage. Thus the magnetic field distribution around the cable surface at a certain location along the cable is also proportional to the supply voltage. As such, the magnetic field distribution around the cable surface at the head (power supply side) and tail (load side) ends of the power cable was also calculated at other typical voltages (7.2, 11, 12.47, 22, 25, 34.5 kV [24]) at 50 Hz. Fig. 8(a) and (b) show the magnetic field distribution around the cable surface at the head and tail ends of the 600-m cable at various supply voltages. The result shows that the magnitude of the magnetic fields increases with the increasing voltages. The pattern of three peaks and three troughs is obvious in all the simulated magnetic field distributions.

(b) Cable length: according to Eq. 11, the magnitude of the charging current is proportional to the cable length. As such, the magnetic field distribution around the cable surface at a certain section is also proportional to the cable length. In practice, the length of the power cable can range from hundreds to thousands of meters [34, 35]. The magnetic field distributions around the cable surface at the head and tail end of the power cable of the other cable lengths (1000 m, 2000 m, 3000 m, and 4000 m) were attained from the simulated 600-m one as shown in Fig. 8(c) and (d). The magnitude of the magnetic field increases with the increasing cable lengths and the pattern of three peaks and three troughs is obvious in all the simulated magnetic field distributions.

(c) Power supply frequency: according to Eq. 11, the magnitude of the charging current is proportional to the power supply frequency. The 60 Hz frequency is typically used in the US, and 50 Hz in Europe [24]. For the studied case regarding a 600-m length 22-kV power cable in Fig. 6, the charging current at 60 Hz was also simulated and the results are shown in Fig. 9. It can be seen that the charging current at same measuring point of 60 Hz is 6/5 times as much as that of 50 Hz. Therefore, the magnetic fields around the cable surface at 60 Hz follow the same magnetic-field-distribution pattern as that at 50 Hz but with magnitude 6/5 times larger.

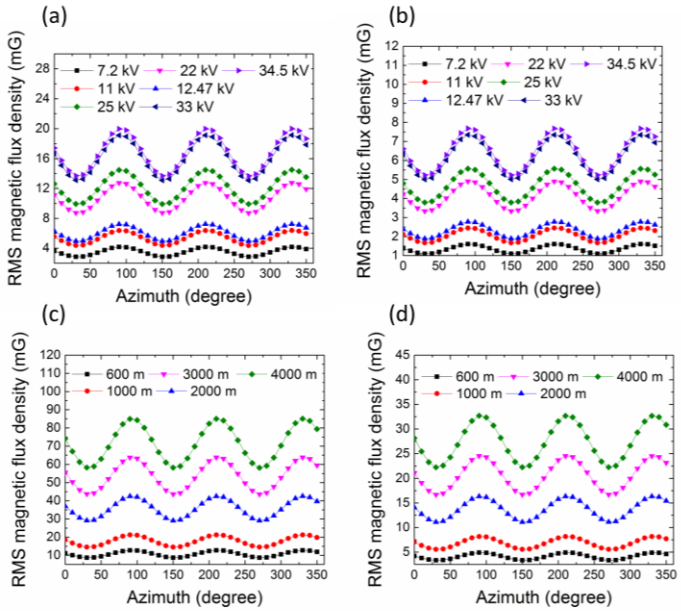

Fig. 8. Magnetic field around the voltage-energized cable surface at various power supply voltages (7.2, 11, 12.47, 22, 25, 33, and 34.5 kV) and cable lengths (600, 1000, 2000, 3000, and 4000 m). (a) Magnetic field at the head end (power supply side) of a 600-m cable at various voltages. (b) Magnetic field at the tail end (load side) of a 600-m cable at various voltages. (c) Magnetic field at the head end of a 22-kV cable of various cable lengths. (d) Magnetic field at the tail end of a 22-kV cable of various cable lengths.

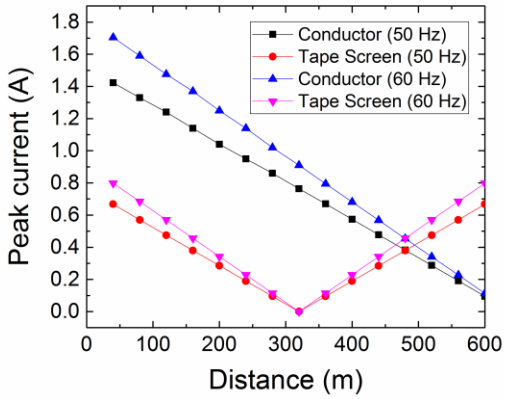

Fig. 9. Charging currents of phase conductor and tape screen at various positions (i.e., various distances from power supply side) on a 600-m power cable at 50 and 60 Hz.

This article has been accepted for publication in a future issue of this journal, but has not been fully edited. Content may change prior to final publication. Citation information: DOI 10.1109/JSEN.2017.2756905, IEEE Sensors Journal

As such, the pattern of three peaks and three troughs still exist around the cable surface for the magnetic fields measured around the cable surface when the cable is voltage-energized. The magnitude of the magnetic fields depends on the cable voltage, length and the measured distance from the power supply. Based on the simulation on various scenarios, the magnitude of the magnetic fields can range from several to tens of mG.

C. De-energized status

In principle, magnetic field does not exist around the cable surface when the power cable is de-energized (i.e., disconnected from the power supply) because there is no load current or charging current. However, current can still arise on the power cable as the grounding electrodes at front and back ends of the cable can be at different Earth potentials (V_F and V_B in the Fig. 10(a)) [36, 37], forming a current loop among the power cable, the grounding electrodes and the Earth (Fig. 10(b)). This current (I) induced by the Earth potential difference can be calculated as

$$I = \frac{V_F - V_B}{2R_e + R_p} = \frac{\nabla V}{2R_e + R_p} \tag{12}$$

$$R_p = \frac{1}{R_s} + \frac{1}{R_{ts\_A}} + \frac{1}{R_{ts\_B}} + \frac{1}{R_{ts\_C}} \tag{13}$$

where ∇V represents the Earth potential difference between the front end (V_F) and back end (V_B), R_e denotes the resistance of the electrode, R_s denotes the resistance of the metallic sheath, and $R_{ts\_A}, R_{ts\_B}, R_{ts\_C}$ denotes the resistance of tape screen of three phases, respectively. By substituting the resistances of the sheath, the tape screen and the electrodes (1 Ω was taken as an example referring to [38]), the current flowing on the sheath and the tape screen with various Earth potential differences is calculated as shown in Fig. 11. Since the cross-sectional area of the sheath is much larger than the tape screen of each phase, the resistance of the sheath is thus much smaller than that of the tape screen. As such, the current flowing on the sheath is much larger than that on the tape screen of each phase. Also, the magnitude of current increases with the Earth potential difference ∇V. Considering the above, the RMS magnetic-field-distribution pattern around the surface of a de-energized cable as a function of azimuth was simulated by FEM as shown in Fig. 12. The RMS magnetic-field-distribution pattern around the cable surface is weak with several mG. More importantly, the pattern of three peaks and three troughs is not observable any more. This is because most current incurred is due to the Earth potential difference (instead of power supply voltage), and it mainly flows through the metallic sheath of the cable rather than through the tape screen of each individual conductor. Therefore, the RMS magnetic-field-distribution around the cable surface around the cable surface as a function of azimuth does not exhibit the pattern with three crests and three troughs. Instead, it is simply flat with the magnitude of several mG.

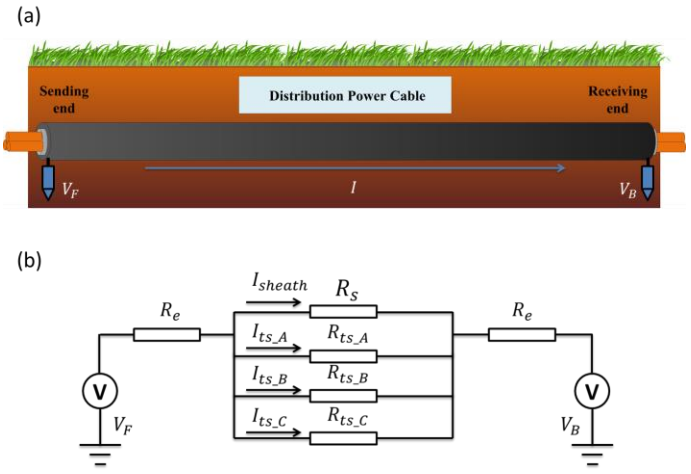

Fig. 10. Current incurred due to the Earth potential difference at the front (V_F) and back (V_B) ends of the cable. (a) Current loop forms among the cable, grounding electrodes, and the Earth. (b) Equivalent electric circuit for calculating the current on the metallic sheath and the tape screens.

Based on the above analysis, an energized three-phase three-core distribution power cable can be identified through the RMS magnetic-field-distribution pattern around the cable surface as a function of azimuth by observing its pattern with three crests and three troughs (Fig. 13). For a de-energized cable, the magnetic field distribution around the cable surface as a function of the azimuth is flat without any pattern. In most normal cases, the current- and voltage-energized statuses can be further distinguished as the magnitude of the current-energized status is from hundreds to thousands of mG while the voltage-energized one is merely from several to tens of mG. Only under some rare extreme cases where the current-energized cable with very light load current (e.g. several amperes) or the voltage-energized cable with very long length (e.g. a 22-kV cable with 4000 m length) that the current-energized status cannot be distinguished from the voltage-energized status because both of their magnetic fields at the cable surface would be in the order of tens of mG. However, the load current of the cable is typically at least tens to hundreds of amperes [27], and thus the magnitude of the magnetic field around the surface of a current-energized cable would be from hundreds to thousands of mG. As such, the current-energized status (i.e., hundreds to thousands of mG) should be distinguishable from the voltage-energized status (i.e., several to tens of mG) under most normal circumstances. It should be noted that the three peaks (troughs) in the magnetic-field-distribution pattern are of the same magnitude since the analysis in Section II(A) and (B) assumes that the three phase conductors are perfectly symmetric and the distance between each conductor to the cable center is the same. Nevertheless, in reality the three phase conductors are not necessarily symmetric and the distance between each conductor and the cable center is not ideally the same and thus the three peaks (troughs) may not be of exactly the same magnitude.

This article has been accepted for publication in a future issue of this journal, but has not been fully edited. Content may change prior to final publication. Citation information: DOI 10.1109/JSEN.2017.2756905, IEEE Sensors Journal

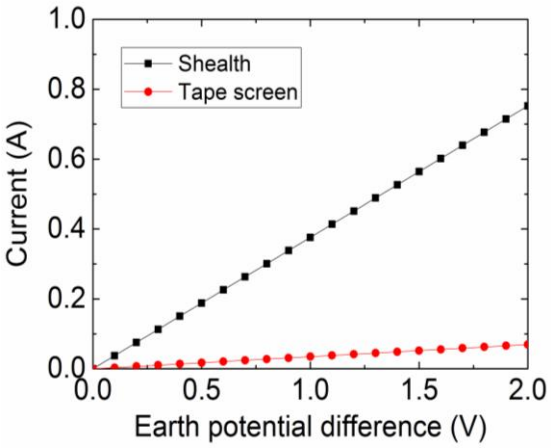

Fig. 11. Current flowing on the sheath and tape screen with various Earth potential differences from 0 to 2 V.

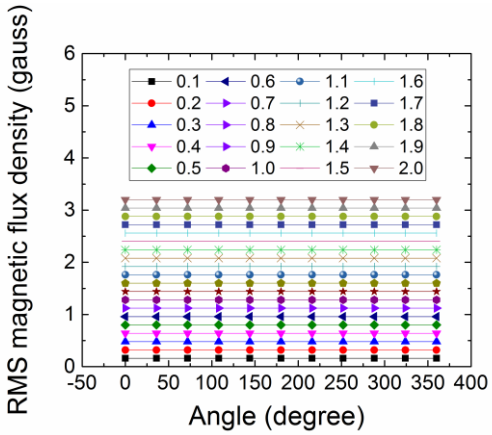

Fig. 12. RMS magnetic-field-distribution pattern around the de-energized cable surface measured at 60 mm from the cable center with various Earth potential difference ∇V (0.1 V, 0.2 V, etc.).

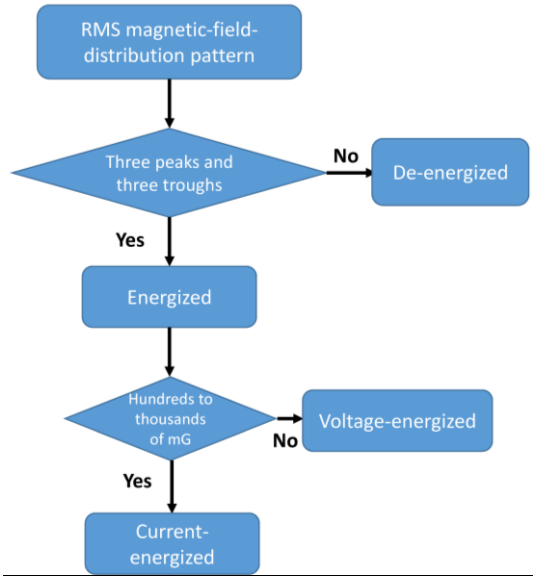

Fig. 13. Identification of energization status of a three-phase three-core distribution power cable from the magnetic-field-distribution pattern around the cable surface. Under most normal circumstances current-energized, voltage-energized and de-energized statuses can all be properly distinguished.

D. Imbalanced current

Due to the imbalance of three-phase loading, the three-phase currents are not perfectly symmetrical in reality. As such, the magnetic field distribution around the cable surface under the imbalanced current situation is studied as follows. The current imbalance degree (M) is calculated in terms of maximum deviation of current in a phase from the mean of three phases and is mathematically denoted as [39]

$$M = \frac{\max|(I_A - I_m),(I_B - I_m),(I_C - I_m)|}{I_m} \times 100\% \qquad (14)$$

where I_A, I_B, and I_C are three-phase currents, and I_m is their mean value. For our cable structure as shown in Fig. 1, different three-phase current settings were simulated for a series of current imbalance degrees in Table II. The current of phase B and C were fixed as 100 A, and the phase A was changed from 100 to 230 A. The current imbalance degree (M) is calculated accordingly based on Eq. (14). The magnetic fields around the cable surface were simulated, and the results shows that the symmetry of three peaks and troughs gradually disappeared with some peaks becoming dominant while some weaker (Fig. 14). It can be seen that three peaks are still observable when the current imbalance degree reaches to as much as 37.8 %. In reality, the current imbalance degree would not exceed 10 % in power system [39] because remedial actions would have already been taken to balance the loads. Therefore, our method is feasible for identifying the current-energized status by observing the three peaks and troughs even under the circumstances of imbalanced phase currents.

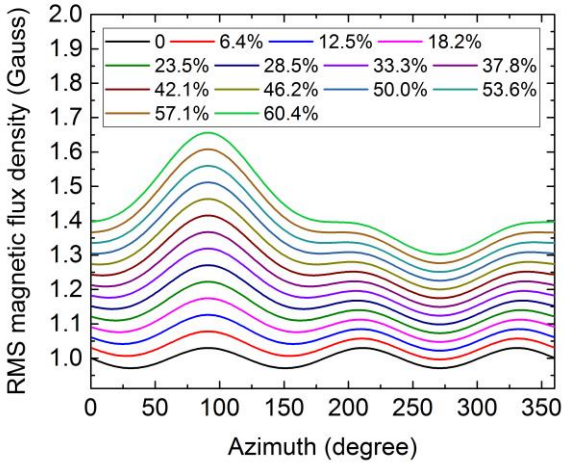

Fig. 14. Magnetic fields around the case surface simulated at various current imbalance degree.

TABLE II Imbalanced three-phase currents for simulating the magnetic-field-distribution around the cable surface

This article has been accepted for publication in a future issue of this journal, but has not been fully edited. Content may change prior to final publication. Citation information: DOI 10.1109/JSEN.2017.2756905, IEEE Sensors Journal

Item	Phase A (A)	Phase B (A)	Phase C (A)	M (%)
1	100	100	100	0
2	110	100	100	6.4
3	120	100	100	12.5
4	130	100	100	18.2
5	140	100	100	23.5
6	150	100	100	28.5
7	160	100	100	33.3
8	170	100	100	37.8
9	180	100	100	42.1
10	190	100	100	46.2
11	200	100	100	50.0
12	210	100	100	53.6
13	220	100	100	57.1
14	230	100	100	60.4

E. Imperfect cable geometry

(a) Imbalanced angle difference

In fact, the three-phase conductors are not perfectly symmetrical at 120° [32]. From the result at Section II(A), the magnetic-field pattern around the cable surface also depends on the spatial position of conductors. As such, the asymmetry of the three-phase conductors at various angle difference is studied. The layout of the three-phase conductor is shown in Fig. 15(a), where the position of phase B and C are fixed while the position of phase A is rotated angularly (the angular degree between phase A and horizontal axis is θ) to illustrate the asymmetry. Similarly, the angle imbalance degree (N) is calculated in terms of maximum deviation of angle between adjacent two phases ($\theta_{AC}, \theta_{AB}, \theta_{BC}$) from their mean value, and it is mathematically denoted as [39]

$$N = \frac{\max|(\theta_{AC}-\theta_m),(\theta_{AB}-\theta_m),(\theta_{BC}-\theta_m)|}{\theta_m} \times 100\% \qquad (15)$$

where θ_m is the mean value of θ_{AC}, θ_{AB} and θ_{BC}. With the position of phase A changed angularly, the angle between adjacent two phases and the angle imbalance degree for simulation were calculated in Table III. The magnetic fields around the cable surface for the studied case in Fig. 1 are shown in Fig. 15 (b), (c) and (d). The result shows that the three peaks and troughs are still observable when the angle imbalance degree does not exceed 33%. In fact, the value of 33% angle imbalance is very unlikely to occur in reality because the three-phase conductors are laid very compactly in the space as shown in Fig. 16 where the angle imbalance degree is 5.8%. Therefore, our method is feasible even when the cable conductors are not spaced perfectly symmetrically.

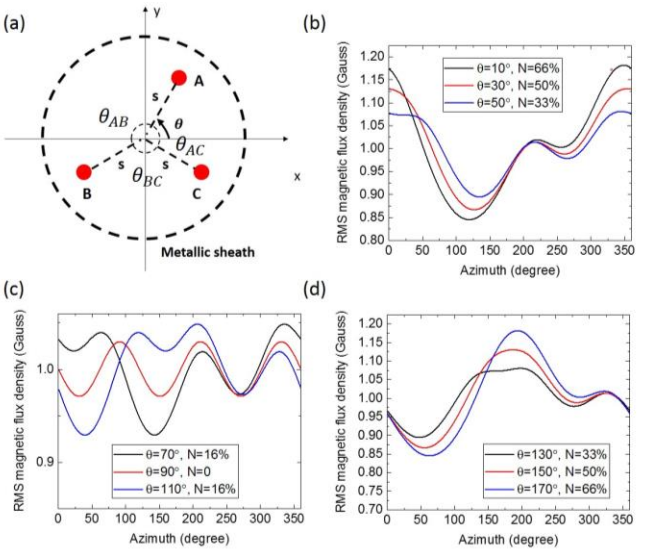

Fig. 15. Study of imbalanced cable geometry. (a) Positions of phase B and C are fixed while phase A are rotated angularly. (b) Magnetic fields around the cable surface at various locations of phase A ($\theta = 10°$, N=66%; $\theta = 30°$, N=50%; $\theta = 50°$, N=33%). (c) Magnetic fields around the cable surface at various locations of phase A ($\theta = 70°$, N=16%; $\theta = 90°$, N=0; $\theta = 110°$, N=16%). (d) Magnetic fields around the cable surface at various locations of phase A ($\theta = 130°$, N=33%; $\theta = 150°$, N=50; $\theta = 170°$, N=66%).

TABLE III Various angle imbalance degree of a three-phase power cable

Angle (θ°)	θ_{AC} (°)	θ_{AB}(°)	θ_{BC}(°)	N (%)
10	40	200	120	66
30	60	180	120	50
50	80	160	120	33
70	100	140	120	16
90	120	120	120	0
110	140	100	120	16
130	160	80	120	33
150	180	60	120	50
170	200	40	120	66

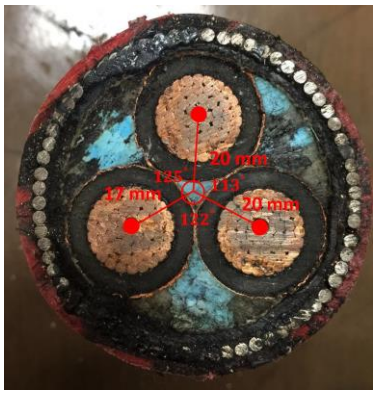

Fig. 16. Sectional image of a three-phase power distribution cable for asymmetry information.

(b) Imbalanced phase distance

This article has been accepted for publication in a future issue of this journal, but has not been fully edited. Content may change prior to final publication. Citation information: DOI 10.1109/JSEN.2017.2756905, IEEE Sensors Journal

The distance between the phase conductor center and the cable center may not be the same for each conductor. The distance imbalance degree (K) is calculated in terms of maximum deviation of distance to center of a phase from the mean of distances of three phases, and is mathematically expressed as

$$K = \frac{\max|(S_1 - S_m),(S_2 - S_m),(S_3 - S_m)|}{S_m} \times 100\% \quad (16)$$

where S_1, S_2 and S_3 are the distance of each phase-conductor center to each phase conductor's center to the cable center as shown in Fig. 17(a), and S_m is their mean value. In order to study the magnetic-field pattern around the cable surface under various distance imbalance degree, various distances from each phase-conductor center to the cable center were set in the simulations as shown in Table IV. The magnetic-field patterns under various distance imbalance degrees are shown in Fig. 17(b), (c) and (d). The result shows that the peak can disappear when the position of some phase-conductor center is too close to the cable center (e.g., K=36%), namely, being far away from the magnetic field sensing point on the cable surface. However, from the point of view of cable physical structure, it is very unlikely for this extreme level of distance imbalance to occur. For reference, the distance imbalance degree for the cable shown in Fig. 16 is 10.5%. Therefore, our method is feasible even under circumstances of imbalanced phase distance.

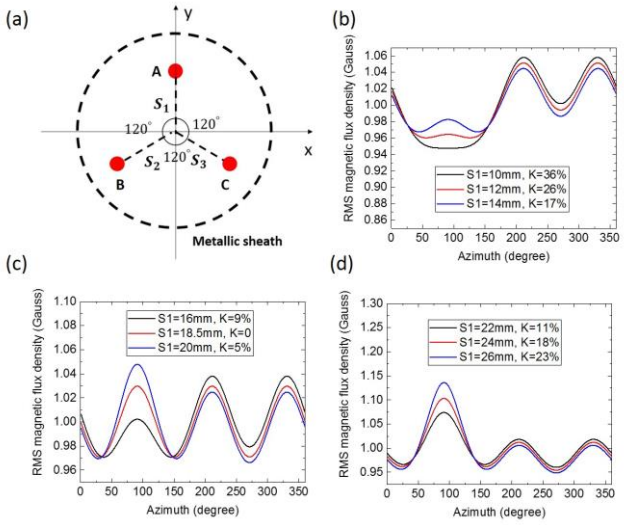

Fig. 17. Study of imbalanced phase distance. (a) Distance between phase B and C to the center is fixed ($S_2 = S_3 = 18.5\ mm$) while distance between Phase A to the center (S_1) is changed. (b) Magnetic fields around the cable surface at various distances between phase A and the cable center ($S_1 = 10$ mm, K=36%; $S_1 = 12$ mm, K=26%; $S_1 = 14$ mm, K=17%). (c) Magnetic fields around the cable surface at various distances between phase A and the cable center ($S_1 = 16$ mm, K=9%; $S_1 = 18.5$ mm, K=0; $S_1 = 20$ mm, K=5%). (d) Magnetic fields around the cable surface at various distances between phase A and the cable center ($S_1 = 22$ mm, K=11%; $S_1 = 24$ mm, K=18%; $S_1 = 26$ mm, K=23%).

TABLE IV Various distance imbalance degree of a three-phase power cable

S_1(mm)	S_2(mm)	S_3(mm)	K (%)
10	18.5	18.5	36
12	18.5	18.5	26
14	18.5	18.5	17
16	18.5	18.5	9
18.5	18.5	18.5	0
20	18.5	18.5	5
22	18.5	18.5	11
24	18.5	18.5	18
26	18.5	18.5	23

III. MAGNETIC-FIELD-SENSING PLATFORM

The platform was designed accordingly for measuring the magnetic field distribution around the cable surface, and the overall system structure is shown in Fig. 18. Four magnetoresistive (MR) sensors (HMC2003, Honeywell) providing high sensitivity and spatial resolution were installed to measure the magnetic-field-distribution pattern around the cable surface as a function of the azimuth. A triple-layered magnetic shielding was designed to eliminate background interference such as the Earth's magnetic fields and the magnetic fields emanated from the adjacent in-service cables. The measured data were acquired by a data acquisition (DAQ) card (NI USB-6211) and then processed by a LabVIEW program [40]. The details about the key component (i.e., MR sensors and shielding) are as follows.

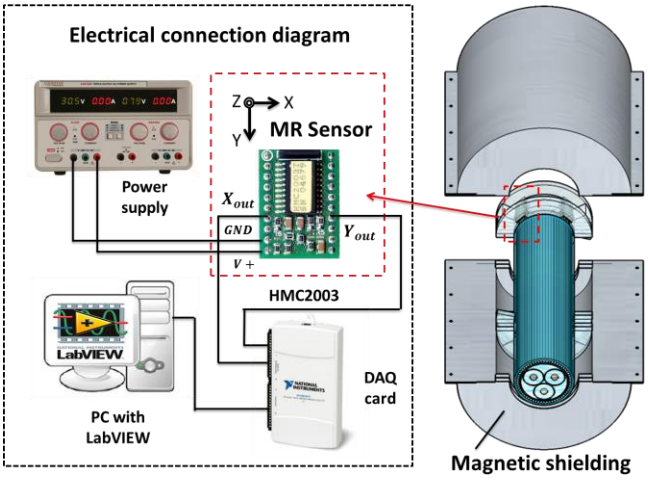

Fig. 18. Schematic diagram for the overall magnetic-field-sensing platform comprised of MR sensors, triple-layer magnetic shielding, and data acquisition (DAQ) system.

1) MR sensors

Most of the MR sensors are either 1- or 3- axis sensors [19, 41]. As shown in Fig. 19, the vectors of the resultant magnetic fields around the multi-core cable surface at various points are not necessarily tangential (e.g., B_{sum} and $B_{sum}{}'$) but forms different angles (e.g., θ_1 and θ_2) with regard to the cable center. Therefore, the MR sensors with mutually orthogonal sensing axes in a plane (B_t and B_n) are needed for reconstructing the resultant magnetic field. As such, the 3-axis MR sensors are deployed with one sensing axis along B_t, one along B_n and the

This article has been accepted for publication in a future issue of this journal, but has not been fully edited. Content may change prior to final publication. Citation information: DOI 10.1109/JSEN.2017.2756905, IEEE Sensors Journal

remaining one aligned with the cable direction. In our experiment to verify the principle, the Honeywell MR sensor HMC2003 was used which provides a 40–μG resolution to measure low magnetic field less than 2 G. The output of the sensor is voltage, which is proportional to the strength of the magnetic field. The sensor is calibrated, and its sensitivity is consistent with the value provided by the datasheet, i.e., 1 V/gauss [42]. The sensor resolution is sufficiently high for detecting the weak magnetic field (several to tens of mG) for voltage-, and de-energized power cables, and the 2-gauss range enables the platform to measure the power cable with rated current from 4 mA to 200 A according to Section II(A). The four compact-in-size HMC2003 were positioned orthogonally to each other and the magnetic flux density around the cable surface as a function of azimuth can be measured by rotating them (Fig. 20).

2) Magnetic shielding

Magnetic shielding was designed to reduce magnetic interference from the background. For a single-layered magnetic shielding (blue ring in Fig. 21(a)), the attenuation ratio (incident magnetic field B_i over the transmitted field B_t) for the DC field is calculated as

$$\left|\frac{B_i}{B_t}\right| \approx \frac{\mu_r(r_{1o}-r_{1i})}{2r_{1o}} \quad (17)$$

where μ_r is the permeability of the shielding material, r_{1i} and r_{1o} are the inner and outer radius of the shielding, respectively. The larger the attenuation ratio, the better the shielding effectiveness. In order to achieve a larger attenuation ratio, the high-permeability Mu-metal ($\mu_r \approx 10^4 \sim 10^5$) was adopted. This is because the high-permeability material directs the magnetic field lines through the alloy and thus keeping the external magnetic field lines away from the sensing zones where the MR sensors are located. The thickness of 1 mm was adopted considering both the attenuation ratio and the shielding weight. The inner radius of 95 mm was designed for reserving enough room to install the sensor array. In order to enhance the shielding effectiveness, the single-layered shielding (blue ring in Fig. 21(a)) was further modified into triple layers (blue and grey rings in Fig. 21(a)). The relation between the attenuation ratio and the interval spacing between adjacent layers (d) is shown in Fig. 21(b). The result shows that the larger the interval spacing, the higher the attenuation ratio; however, the overall shielding size would become larger. The spacing of 30 mm was adopted for the triple-layered magnetic shielding as a compromise considering both the attenuation ratio and the overall shielding size. Then the Mu-metal triple-layered magnetic shielding was fabricated and experimentally tested as shown in Fig. 21(c), in which an external uniform magnetic field was generated by a pair of coils. An external DC magnetic field of 0.5 G was applied and the magnetic flux density at the center of the shielding was measured to be 3.44×10^{-5} G, i.e., an attenuation ratio of 1.5×10^4, indicating an effective shielding performance in DC condition.

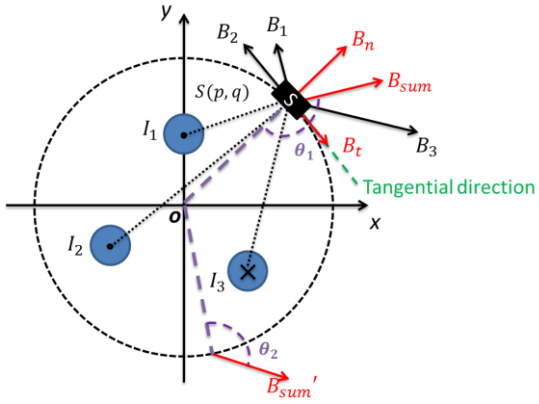

Fig. 19. Magnetic field vector generated by three-phase current in a three-phase power distribution cable.

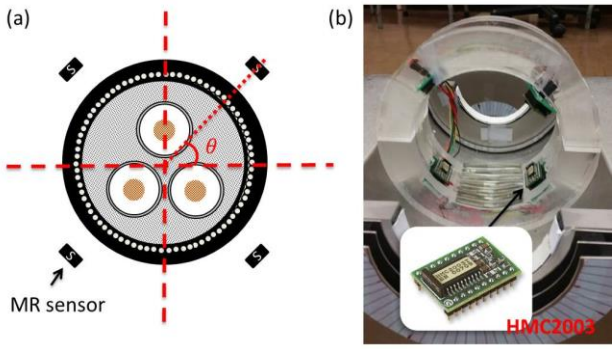

Fig. 20. MR sensors installed (60mm from the cable center) for measuring the magnetic flux density around the cable surface. (a) Schematic diagram of MR sensors and the cable. (b) MR sensors (HMC2003).

The AC magnetic interference also exists in the actual on-site environment because the in-service power cables (mainly operating at 50 or 60 Hz) are typically installed neighboring each other. Therefore, the triple-layered shielding was also evaluated under the AC conditions. A 4 Gauss magnetic field was applied at various frequencies (10 – 60 Hz) both in FEM simulation and experiment, and the relation between the attenuation ratio and the frequency is shown in Fig. 21(d). Both the FEM and experimental results show that the attenuation ratio under AC conditions (~ hundreds at 10 Hz) is lower than that under DC condition. This is because the eddy currents are induced which generate the extra magnetic field inside the shielding [43]. The eddy currents become stronger with increasing frequency, and thus the attenuation ratio decreases with frequency. Nevertheless, the shielding can still function at 50 Hz (60 Hz) frequency with an attenuation ratio of around 50 (40) in the experiment. Therefore, the triple-layered magnetic shielding made of Mu-metal can reduce both the DC and AC magnetic interferences effectively.

This article has been accepted for publication in a future issue of this journal, but has not been fully edited. Content may change prior to final publication. Citation information: DOI 10.1109/JSEN.2017.2756905, IEEE Sensors Journal

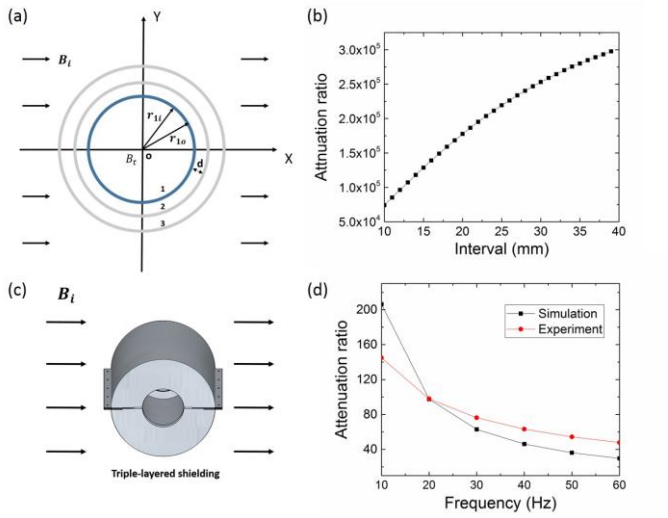

Fig. 21. Design of a triple-layered magnetic shielding for reducing the background magnetic noise. (a) Structure of single- and triple-layered magnetic shielding. (b) Simulation of attenuation ratio with various spacing for a triple-layered magnetic shielding (μ_r=30000, r_{1i}= 95 mm, and thickness is 1 mm) under DC conditions. (c) Experimental test of the triple-layered shielding for verifying the attenuation ratio. (d) FEM simulation ($\sigma_r = 1.61\times10^7$ s/m) and experiment results for the attenuation ratio of the shielding under AC.

IV. ONSITE EXPERIMENT

An onsite experiment was conducted to verify the proposed identification technique in a substation. The substation bridges the transmission and distribution network with 4 × 60 MVA transformers by stepping down the voltage from 275 kV to 22 kV, and then transmit electricity to the load side through these three-phase three-core armored 22-kV XLPE stranded distribution power cables [44].

The shielding performance was validated onsite before measurement. The magnetic flux density measured by the Gauss-meter (DT-1130 manufactured by PWOW®) near the target cable in the cable room of the substation was 0.61 μT (Fig. 22(a)). The reading dropped to 0.00 μT (Fig. 22(b)) when the Gauss-meter was shielded by the triple-layered shielding, showing that the shielding can effectively suppress external interferences in the real onsite environment.

The platform was installed on a three-phase three-core armored 22-kV XLPE stranded distribution power cable as shown in Fig. 23, where the platform was installed about 200 m from the power supply side (the total cable length is approximately 650 m). The platform was rotated so that the MR sensor array could measure the magnetic field distribution around the cable surface with the target power cable in energized (current- and voltage-energized) and de-energized statuses respectively. The RMS magnetic-field-distribution pattern around the cable surface as a function of azimuth under current-, voltage-, and de-energized status is shown in Fig. 24. The energized status of the power cable can be identified through the observable pattern with three crests and three troughs. The magnetic flux under current-energized status exhibited small random fluctuation due to the real-time demand change from the load side during the measurement. The real-time three-phase currents measured by the CT during the experiment is shown in Table. V. The RMS magnetic flux densities under current-energized status were on the level of hundreds of mG (average 344.1 mG) as expected for the load current of around 30 A according to the analysis in Section II(A). Moreover, the average magnitude for the voltage-energized status was 13.2 mG, which is 26 times lower than the magnitude under current-energized status for this 650-m 22-kV three-phase three-core distribution power cable. There exhibited no random fluctuation in the waveform since the charging current only depends on the power supply voltage, cable type and length which do not change over time. The three peaks (troughs) are not of the same magnitude in the magnetic-field pattern due to the fact that the positions of the three-phase conductors are not perfectly symmetrical at 120° in a real cable (referred to the discussion in Section II(E)). As shown in the Fig. 24, the peaks are almost spaced by 105°, 104° and 151° apart, rather at 120 ° intervals. The RMS magnetic-field-distribution pattern around the cable surface as a function of azimuth in the de-energized status was flat with the magnitude of several mG. The experimental results verified the analysis in Section II, and the energized power cable can be successfully identified from the de-energized status by the proposed technique. Furthermore, voltage-energized and current-energized statuses can also be distinguished in this onsite experiment.

TABLE V. MEASURED CURRENT FOR EACH PHASE OF DISTRIBUTION POWER CABLE DURING THE EXPERIMENT

	Time (hh:mm)	Phase A (A)	Phase B (A)	Phase C (A)
Measured by current transformer	12:03	32.50	33.75	35.00
	12:13	31.60	33.00	34.00
	12:23	31.75	32.50	34.50
	12:33	32.00	33.80	35.00
	12:43	33.60	34.00	37.00
	12:53	32.50	32.75	34.25
	Average	32.32	33.30	34.95

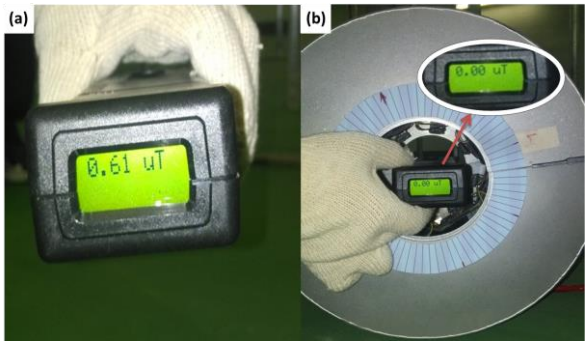

Fig. 22. Verification of shielding performance in the cable room. (a) Magnetic flux density measured without shielding. (b) Magnetic flux density measured with shielding.

This article has been accepted for publication in a future issue of this journal, but has not been fully edited. Content may change prior to final publication. Citation information: DOI 10.1109/JSEN.2017.2756905, IEEE Sensors Journal

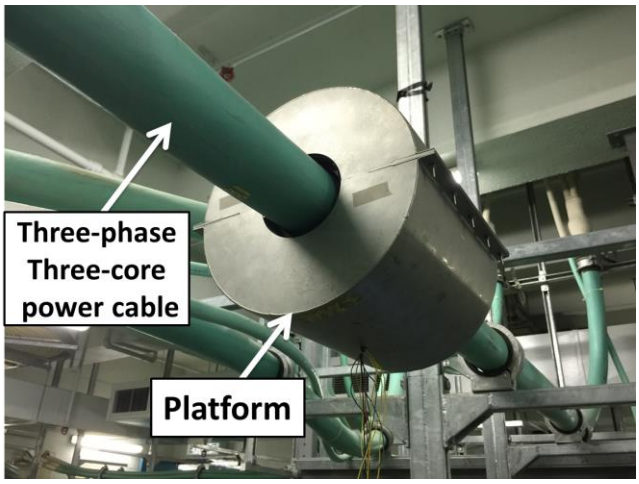

Fig. 23. Magnetic-field-sensing platform installed on a 22-kV three-phase three-core distribution power cable inside the cable room of a substation.

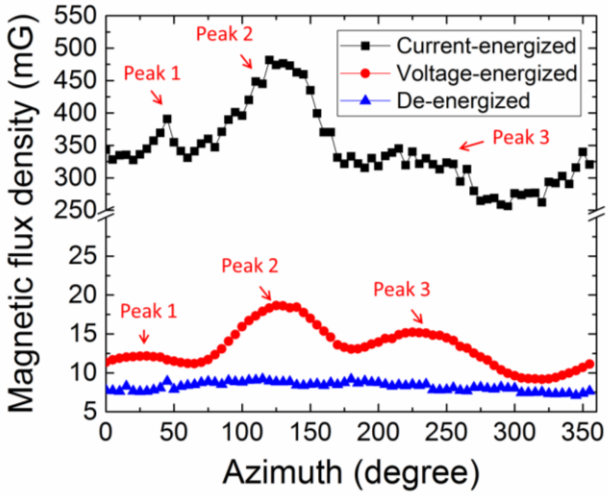

Fig. 24. RMS magnetic flux densities as a function of azimuth around the cable surface for current-, voltage-, and de-energized status of the three-phase three-core power cable from on-site measurement.

V. Conclusion

In this paper, a magnetic-field-sensing based technique for non-destructively identifying the energization status of the three-phase three-core distribution power cables was proposed. The RMS magnetic-field-distribution pattern around the cable surface as a function of azimuth around the surface of an energized cable (voltage-energized or current-energized) was found to exhibit a pattern with three peaks and three troughs which is very distinguishable from the flat pattern for de-energized power cables. This technique was validated experimentally on-site on the three-phase three-core armored 22-kV XLPE stranded distribution power cables. The proposed method is non-contact since the magnetic field distribution pattern is not shielded by the earthed metallic sheath within cables and thus can be sensed on the cable surface. In this way, the cable integrity is maintained and the risk of endangering the lives of repair crew is totally avoided. The triple-layered shielding can effectively eliminate the external magnetic interference and enhance the reliability of the sensing platform in the on-site environment.

Though there might be concern about short cable length or the condition of ungrounded cable sheath for the feasibility of the proposed method, these situations rarely exist in reality. Regarding the cable length issue, the magnetic signals are weaker for shorter cable under voltage-energized status. The magnitude of magnetic signal shall not be smaller than the sensor's detection resolution. In our case, considering the fact that (a) the weakest magnetic field under the voltage-energized status of the 600-m 22-kV cable is about 3 mG (Fig. 7) and (b) the resolution of the magnetoresistive sensor HMC2003 is 40 μG [42], the minimum cable length can be calculated to be 600 m × (40 μG / 3 mG) = 8 m. However, in practice, distribution cable lengths are typically from tens to thousands of meters [45, 46]; it is extremely unlikely to have a distribution cable less than 8 m in length. Regarding the ungrounded-cable-sheath issue, it is a widely adopted code of practice [45, 46] that the cable sheath must be grounded in at least one point for safety reasons (e.g., limit sheath voltage, reduce sheath losses to a minimum, maintain a continuous sheath circuit for fault current return, etc.) [45, 46]. This creates potential difference on the cable sheath and results in the charging current flowing on the cable sheath, providing three peaks and troughs pattern for voltage-energized status. Therefore, the proposed method shall work robustly.

Future work will focus on extending the magnetic sensors to a denser sensor array with more MR sensors to expedite the measuring process. Currently there is an array of only four MR sensors installed in this prototype, thus the platform has to be rotated for measuring the magnetic-field pattern in a full circle around the cable surface. In the future, the rotation process will be completely eliminated by building a denser MR magnetic sensor array with 36 miniatured MR sensors (e.g., to use 3-axis MR sensors *HMC1043L (Honeywell)* [47] with the dimension of 3.3 mm × 2.8 mm × 1.1 mm or 3-axis MR sensor *TMR2301(MultiDimension)* [48] with the dimension of 5.0 mm × 5.0 mm × 2.5 mm for forming a circular array). With this new version of measurement platform composed of 36 MR sensors, we will be able to complete the measurement of magnetic field around the cable surface instantaneously without any rotation, and the magnetic-field pattern will be obtained immediately.

VI. Reference

[1] S. Foss, S. Lin, R. Maraio, and H. Schrayshuen, "Effect of variability in weather conditions on conductor temperature and the dynamic rating of transmission lines," *IEEE Trans. Power Del.*, vol. 3, pp. 1832-1841, 1988.

[2] M. Lehtonen, "Fault rates of different types of medium voltage power lines in different environments," in *the Elec. Pwr. Qual. Sply. Relia Conf.*, 2010, pp. 197-202.

[3] G. J. Anders, I. o. Electrical, and E. Engineers, *Rating of electric power cables in unfavorable thermal environment*: Wiley, 2005.

[4] L. Bertling, R. Allan, and R. Eriksson, "A reliability-centered asset maintenance method for assessing the impact of maintenance in power distribution systems," *IEEE Trans. Power Syst.*, vol. 20, pp. 75-82, 2005.

[5] T. Kubota, Y. Takahashi, S. Sakuma, M. Watanabe, M. Kanaoka, and H. Yamanouchi, "Development of 500-kV XLPE cables and accessories for long distance underground transmission line-Part I: insulation design of cables," *IEEE Trans. Power Del.*, vol. 9, pp. 1741-1749, 1994.

[6] A. Ukil, H. Braendle, and P. Krippner, "Distributed temperature sensing: review of technology and applications," *IEEE Sensors J.*, vol. 12, pp. 885-892, 2012.

[7] R. H. Bhuiyan, R. A. Dougal, and M. Ali, "Proximity coupled interdigitated sensors to detect insulation damage in power system cables," *IEEE Sensors J.*, vol. 7, pp. 1589-1596, 2007.

[8] F. Li, W. Qiao, H. Sun, H. Wan, J. Wang, Y. Xia, Z. Xu, and P. Zhang, "Smart transmission grid: Vision and framework," *IEEE Trans. Smart Grid*, vol. 1, pp. 168-177, 2010.

[9] S. L. Christopherson, E. C. Gillard, D. A. Gilliland, and K. E. Monsen, "Device and method for directly injecting a test signal into a cable," ed: Google Patents, 2004.

[10] T. D. Walsh, N. Reinhardt, and J. M. Feldman, "Cable status testing," ed: Google Patents, 1988.

[11] SebaKMT. *'Principles of Cable & Pipe Location', 2011.* Available: http://www.ausolutions.com.au/pdf-library/vLocPro-Theory-Presentation_V1-41.pdf. [Accessed: 12- Dec- 2016].

[12] SPIKE. *'SPIKE Tool Speficiations', 2005.* Available: http://www.spiketool.com/SPIKEhome.html. [Accessed: 12- Dec- 2016].

[13] T. Walsh and T. Feldman. *"Shielded cable is tested to determine if it is energized", 2006.* Available: http://ieeepcic.com/wp-content/uploads/2016/10/Test-Before-Touch-PCIC-2006.pdf. [Accessed: 12- Dec- 2016].

[14] B. Jiang, A. P. Sample, R. M. Wistort, and A. V. Mamishev, "Autonomous robotic monitoring of underground cable systems," in *the 12th Intl. Conf. on Advanced Robotics*, 2005, pp. 673-679.

[15] S. Cristina and M. Feliziani, "A finite element technique for multiconductor cable parameters calculation," *IEEE Trans. Magn.*, vol. 25, pp. 2986-2988, 1989.

[16] P. Klaudy and J. Gerhold, "Practical conclusions from field trials of a superconducting cable," *IEEE Trans. Magn.*, vol. 19, pp. 656-661, 1983.

[17] S. Short, A. Mamishev, T. Kao, and B. Russell, "Evaluation of methods for discrimination of energized underground power cables," *Electr. Pow. Syst. Res.*, vol. 37, pp. 29-38, 1996.

[18] A. B. Gill, Y. Huang, J. Spencer, and I. Gloyne-Philips, "Electromagnetic fields emitted by high voltage alternating current offshore wind power cables and interactions with marine organisms," in *Proc. of the Electromag. in Current and Energy*, 2012.

[19] J. Lenz and S. Edelstein, "Magnetic sensors and their applications," *IEEE Sensors J.*, vol. 6, pp. 631-649, 2006.

[20] H. Kaimori, A. Kameari, and K. Fujiwara, "FEM computation of magnetic field and iron loss in laminated iron core using homogenization method," *IEEE Trans. Magn.*, vol. 43, pp. 1405-1408, 2007.

[21] G. Ries and S. Takács, "Coupling losses in finite length of superconducting cables and in long cables partially in magnetic field," *IEEE Trans. Magn.*, vol. 17, pp. 2281-2284, 1981.

[22] C. Schifreen and W. Marble, "Charging Current Limitations in Operation or High-Voltage Cable Lines [includes discussion]," *Trans. of the American Inst. of Elect. Eng.*, vol. 75, 1956.

[23] E. Ghafar-Zadeh and M. Sawan, "Charge-based capacitive sensor array for CMOS-based laboratory-on-chip applications," *IEEE Sensors J.*, vol. 8, pp. 325-332, 2008.

[24] Wikipedia. *'Electric power distribution', 2016.* . Available: https://en.wikipedia.org/wiki/Electric_power_distribution. [Accessed: 19- Jan- 2017].

[25] Wikipedia. *'High-voltage cable', 2016.* Available: https://en.wikipedia.org/wiki/High-voltage_cable. [Accessed: 19- Jan- 2017].

[26] F. Moro and R. Turri, "Accurate Calculation of the Right-of-Waywidth for Power Line Magnetic Field Impact Assessment," *Prog. Electromagn. Res.*, vol. 37, pp. 343-364, 2012.

[27] J. Nahman and M. Tanaskovic, "Determination of the current carrying capacity of cables using the finite element method," *Electr. Pow. Syst. Res.*, vol. 61, pp. 109-117, 2002.

[28] H. Li, K. Tan, and Q. Su, "Assessment of underground cable ratings based on distributed temperature sensing," *IEEE Trans. Power Del.*, vol. 21, pp. 1763-1769, 2006.

[29] G. Gela and J. Dai, "Calculation of thermal fields of underground cables using the boundary element method," *IEEE Trans. Power Del.*, vol. 3, pp. 1341-1347, 1988.

[30] P. C. Chao, "Energy harvesting electronics for vibratory devices in self-powered sensors," *IEEE sensors J.*, vol. 11, pp. 3106-3121, 2011.

[31] J.-C. Liu, Y.-S. Hsiung, and M. S.-C. Lu, "A CMOS micromachined capacitive sensor array for fingerprint detection," *IEEE Sensors J.*, vol. 12, pp. 1004-1010, 2012.

[32] V. K. Mehta. *"Underground Cables", 2011.* Available: http://202.74.245.22:8080/xmlui/bitstream/handle/123456789/112/Ch-11.pdf. [Accessed: 12- Dec- 2016].

[33] PRYSMIAN. *"General calculations excerpt from PRYSMIAN's wire and cable engineering guide", 2006.* Available: http://na.prysmiangroup.com/en/business_markets/markets/industrial/downloads/engineering-guide/General_Calculations_Rev_4.pdf. [Accessed: Dec-12- 2016].

[34] J. Lee, H. Ryoo, S. Choi, K. Nam, S. Jeong, and D. Kim, "Signal Processing Technology for Fault Location System in Underground Power Cable," in *IEEE/PES Trans. Dist. Conf.*, 2006.

[35] S. Mukoyama, S. Maruyama, M. Yagi, Y. Yagi, N. Ishii, O. Sato, M. Amemiya, H. Kimura, and A. Kimura, "Development of 500m HTS power cable in super-ACE project," *Cryogenics*, vol. 45, pp. 11-15, 2005.

[36] L. M. Popovic, "Efficient reduction of fault current through the grounding grid of substation supplied by cable line," *IEEE Trans. Power Del.*, vol. 15, pp. 556-561, 2000.

[37] X. Chen, Y. Cheng, X. Wang, S. Shi, and Y. Zhao, "Analysis of current flowing in the ground wire of XLPE cable and modification of grounding mode," *High Volt. Eng.* , vol. 32, pp. 87-88, 2006.

[38] G. Eduful, J. E. Cole, and P. Okyere, "Optimum mix of ground electrodes and conductive backfills to achieve a low ground resistance," in *the 2nd Intl. Conf. On Adaptive Scie. & Tech.*, 2009.

[39] Amickracing. *'Voltage and current unbalance', 2005.* Available: http://www.hvac.amickracing.com/Electrical%20Information/Current%20Unbalance.pdf. [Accessd: 19-June- 2017].

[40] R. Bitter, T. Mohiuddin, and M. Nawrocki, *LabVIEW: Advanced programming techniques*: CRC Press, 2006.

[41] M. J. Caruso, "Applications of magnetoresistive sensors in navigation systems," SAE Technical Paper 0148-7191, 1997.

[42] Honeywell. *"3-Axis magnetic sensor hybrid HMC2003", 2011.* Available: https://physics.ucsd.edu/neurophysics/Manuals/Honeywell/HMC_2003.pdf. [Accessed: 12- Dec- 2016].

[43] K. L. Kaiser, *Electromagnetic shielding*: Crc Press, 2005.

[44] K. Zhu, H. A. N. W, W. K. Lee, and P. Pong, "On-Site Non-Invasive Current Monitoring of Multi-Core Underground Power Cables with a Magnetic-Field Sensing Platform at a Substation," *IEEE Sensors J.*, vol. 17, pp. 1837-1848, 2017.

[45] D. Tziouvaras, "Protection of high-voltage AC cables," in the IEEE Conf. on Advanced Metering, Protection, Control, Communication, and Distributed Resources, 2006.

[46] J. M. Nahman, V. B. Djordjevic, D. D. Salamon, "Grounding effects of HV and MV underground cables associated with urban distribution substations," *IEEE Trans. Power Del.*, vol.17 , pp.111-116 ,2002.

[47] Honeywell. *'Three-axis magnetic sensor HMC1043L', 2013.* Available: http://ow.ly/68m730dJUL1. . [Accessed: 19- Jul- 2017].

[48] Multi-Dimention. *'TMR2301: 3-axis TMR linear sensor', 2017.* Available: http://www.dowaytech.com/en/1877.html. [Accessed: 19- Jul- 2017].

Ke ZHU (S'12) received the B.E. degree in electrical engineering from China Three Gorges University (CTGU), Yichang, China, in 2013, and is pursuing the Ph.D. degree in electrical and electronic engineering (EEE) at the University of Hong Kong (HKU). His current research and academic interests focus on computational electromagnetics, electric power transmission monitoring, and application of magnetoresistive (MR) sensors in smart grid.

Wing Kin Lee received the B.Sc. degree, the M.Sc. degree from the University of Hong Kong, in 1976 and 1988, respectively, and the M.B.A. degree from the Chinese University of Hong Kong in 1990. He is a professional in electrical services and power engineering, and currently as a Senior Teaching Consultant in the University of Hong Kong. He earned industrial experience while involved with power and communication utility companies in Hong Kong. His current research interests include smart grid demand side management, electrical load signature, and vertical transportation.

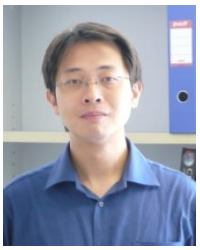

Philip W. T. Pong (SM'13) is a physicist and electrical engineer working on magnetoresistive magnetic field sensors and smart grid at the Department of Electrical and Electronic Engineering (EEE), the University of Hong Kong (HKU). He received a Ph.D. in engineering from the University of Cambridge in 2005. He was a postdoctoral researcher at the Magnetic Materials Group at the National Institute of Standards and Technology (NIST) for three years. In 2008, he joined the HKU engineering faculty as an assistant professor working on tunneling magnetoresistance (TMR) sensors, and the application of magnetoresistive sensors in smart grid.